sustainability

MDPI

Article

Surface Subsidence Response to Safety Pillar Width Between Reactor Cavities in the Underground Gasification of Thin Coal Seams

Ivan Sakhno [1,*], Svitlana Sakhno [1] and Oleksandr Vovna [1,2]

[1] Department of Mining, Mining and Metallurgy Faculty, Technical University "Metinvest Polytechnic" LLC., Pivdenne Shose 80, 69008 Zaporizhzhia, Ukraine; svitlana.sakhno@mipolytech.education (S.S.); oleksandr.vovna@knu.ua (O.V.)

[2] Department of Software Systems and Technologies, Faculty of Information Technology, Taras Shevchenko National University of Kyiv, Volodymyrska Str., 60, 01033 Kyiv, Ukraine

* Correspondence: ivan.sakhno@mipolytech.education

Abstract: Underground coal gasification (UCG) is a clean and automated coal technological process that has great potential. Environmental hazards such as the risk of ground surface subsidence, flooding, and water pollution are among the problems that restrict the application of UCG. Overburden rock stability above UCG cavities plays a key role in the prevention of the mentioned environmental hazards. It is necessary to optimize the safety pillar width to maintain rock stability and ensure minimal coal losses. This study focused on the investigation of the influence of pillar parameters on surface subsidence, taking into account the non-rectangular shape of the pillar and the presence of voids above the UCG reactor in the immediate roof. The main research was carried out using the finite element method in ANSYS 17.2 software. The results of the first simulation stage demonstrated that during underground gasification of a thin coal seam using the Controlled Retraction Injection Points method, with reactor cavities measuring 30 m in length and pillars ranging from 3.75 to 15 m in width, the surface subsidence and rock movement above gasification cavities remain within the pre-peak limits, provided the safety pillar's bearing capacity is maintained. The probability of crack initiation in the rock mass and subsequent environmental hazards is low. However, in the case of the safety pillars' destruction, there is a high risk of crack evolution in the overburden rock. In the case of crack formation above the gasification panel, the destruction of aquiferous sandstones and water breakthroughs into the gasification cavities become possible. The surface infrastructure is therefore at risk of destruction. The assessment of the pillars' stability was carried out at the second stage using numerical simulation. The study of the stress–strain state and temperature distribution in the surrounding rocks near a UCG reactor shows that the size of the heat-affected zone of the UCG reactor is less than the thickness of the coal seam. This shows that there is no significant direct influence of the gasification process on the stability of the surrounding rocks around previously excavated cavities. The coal seam failure in the side walls of the UCG reactor, which occurs during gasification, leads to a reduction in the useful width of the safety pillar. The algorithm applied in this study enables the optimization of pillar width under any mining and geological conditions. This makes it possible to increase the safety and reliability of the UCG process. For the conditions of this research, the failure of coal at the stage of gasification led to a decrease in the useful width of the safety pillar by 0.5 m. The optimal width of the pillar was 15 m.

Keywords: underground coal gasification; pillars stability; surface subsidence; multiple gasification cavities; thin coal seam gasification; safety pillar width

check for updates

Academic Editor: Md. Mizanur Rahman

Received: 13 February 2025
Revised: 3 March 2025
Accepted: 11 March 2025
Published: 13 March 2025

Citation: Sakhno, I.; Sakhno, S.; Vovna, O. Surface Subsidence Response to Safety Pillar Width Between Reactor Cavities in the Underground Gasification of Thin Coal Seams. *Sustainability* **2025**, *17*, 2533. https://doi.org/10.3390/su17062533

---

1. Introduction

In the current century, humanity is on the verge of a global transformation in the energy sector. Global warming requires decisive and effective measures to reduce anthropogenic greenhouse gas emissions. The decarbonization vector is one of the global policy priorities of governments around the world after the Paris Agreement pledges [1], which was also emphasized in 2021 during the COP26 Summit in Glasgow [2].

However, despite the rapid progress of renewables in the last decade and the increase in their share of electricity production to 15%, the role of traditional energy sources is still too high. The energy crisis in Europe in 2022 showed the insufficient pace of the green transition and the impossibility of quickly abandoning fossil fuels [3]. It turned out that the generation of wind power and solar power, which at first provided a jump in green energy, has limited growth potential. Therefore, to further advance the sustainable development of the economic and energy sectors, it is necessary to introduce new green technologies.

Nowadays, coal provides about a quarter of the world's energy generation. The availability of the world's coal reserves is significant (about 55% of major fossil fuels) [4,5]. The dynamics of coal production in the world, unfortunately, still do not show a downward trend. Coal's share of total global energy generation remains around 36% [6]. This is not on track with the Net Zero Scenario. Due to the uneven transition from fossil fuels around the globe, there is a redistribution of coal production, with a shift in its production toward the Asia Pacific region. Traditional coal extraction methods and coal-fired plants cause huge emissions of carbon dioxide and methane. Clean coal technology—specifically, underground coal gasification (UCG)—does not have these disadvantages. This technology ensures the underground conversion of coal into energy and the production of syngas. Gasification occurs at temperatures of more than 1000 °C. During the process of underground coal gasification, voids (UCG reactor cavities) are created. The coal ash and gangue are retained in these UCG voids [7–10]. UCG can be used in coal seams with difficult conditions (low thickness, high ash content, great depth, large bedding angle). At the same time, the risk of accidents, methane gas explosions, and underground rock bursts disappears because UCG is an automated technology. Considering the significant coal reserves on the planet, UCG as a green technology has great potential.

Among the problematic issues that restrict the application of UCG, associated environmental hazards play a significant role. First of all, there is a high risk of ground surface subsidence, flooding, and water pollution due to the fracturing and displacement of overburden above the UCG reactor cavities.

The formation of voids due to coal gasification causes a redistribution of stresses around the reactor cavities, the growth of existing cracks, and the formation of new cracks in the surrounding rock. An additional local change in the stress field during UCG is caused by thermal stress near the reactor. As a result, the roof above the reactor cavities can collapse, forming complex vaulted and dome-shaped cavities [11]. The evolution of these fractures leads to inelastic deformations and the bending of overburden rocks, which can cause UCG fluid emission [12], ground subsidence, and groundwater contamination [13].

Rock stability above UCG reactor cavities plays a key role in preventing environmental hazards. Since artificial support of UCG cavities is not employed, the application of safety pillars between reactors is the only available method of rock stability control. The width of the pillar must be of sufficient size to maintain roof stability, which explains the aspiration to increase it. At the same time, it is desirable to minimize coal losses, which explains the aspiration to reduce the width of the pillars. Therefore, the optimization of pillar width is an important issue [14–16].

Today, there are three main strategies for preventing environmental hazards over goaf: optimizing pillar sizes, filling the goaf, and overburden rock grouting. Goaf filling requires a significant effort in the organization of work and is not implemented currently in underground gasification. Grouting reinforcement construction is only used as a backup (in case of an accident) plan due to its time consumption and high cost. The simplest and cheapest way is to optimize pillar sizes. With optimal pillar sizes, two important conditions are achieved. First, overburden rock retains its bearing capacity and the fracture zone does not reach the aquifers and the surface. This avoids the negative environmental consequences of underground gasification and avoids the risks of destruction for surface infrastructure and groundwater inflow. Second, coal losses in pillars are minimal and gasification efficiency is high. Therefore, this study adopted the strategy of attempting to optimize pillar width.

Many scholars have investigated coal pillar stability during UCG [17,18], as well as strata movement and surface subsidence above UCG reactor cavities [17,19]. The main research method used is numerical simulation. However, these numerical models differ from the conventional models that were used to calculate subsidence during longwall or room-pillar mining, since they take into account the thermal impact on coal and surrounding rocks.

Ranjith et al. [20], Zhang et al. [21], and Wang et al. [22] demonstrated that temperature has a significant effect on rock properties. However, a study presented by Ekneligoda et al. [23] showed that the degradation of the mechanical properties of the rock surrounding the burned zone due to heating has a marginal effect on ground subsidence. Ekneligoda et al. [23] used a coupled thermal-mechanical numerical model to evaluate ground subsidence for single and multiple (parallel) panels.

Therefore, in the case of simulating strata movement and surface subsidence above a UCG reactor, it is permissible to consider temperature only as an additional stress source. Changes in the properties of surrounding rocks in the heating zone are usually neglected.

Wang et al. [24] used a multifield coupled numerical simulation method with three subroutines on the ABAQUS platform to analyze the evolution of thermal-force-chemical-displacement fields after gasification. UCG is simulated using the controlled retraction injection point (CRIP) technology. Yang et al. [25] developed a thermal-mechanical coupled model in ABAQUS software to predict heat transfer, stress distributions around the UCG reactor, and the consequent surface subsidence. Zha et al. [26] used a finite element model coupled with a heat transfer module in COMSOL to simulate the movement of a coal seam roof and surface subsidence during the underground coal gasification process. Lee et al. [27] studied the impact of cave types on ground stability through finite element analysis in PLAXIS 2D. Liu et al. [28] studied the factors that change the rock strata movement and surface subsidence during the underground coal gasification (UCG) process.

Rezaei et al. [29] used numerical analysis, neural networks, fuzzy logic, and statistical analysis to estimate the vertical displacement of the middle and key points of the roof and floor of a UCG cavern under different conditions. Elahi et al. [30] found that the linear elastic model with stress rebalancing can predict rock deformation accurately in the simulation results of the movement and damage of surrounding rock under elastic-plastic models taking into account the thermal-mechanical effect. Jiang et al. [31] studied the influences of the gasification sequence on surface subsidence based on two different scenarios with ANSYS code under the elasticity regime. This study is worthy of attention because it considered not a single reactor cavity but multiple gasification cavities.

Xu et al. [32] analyzed hyperbolic coal pillar stability based on the fact that the shape of pillars during underground gasification differs from rectangular (parallelepiped). Numerical simulations of stress distribution under different stripping degrees, room conditions, and high temperature were used. Li et al. [33] used numerical simulations to investigate how arch height, pillar height and width, and mechanical characteristics affect hyperbolic pillars under the combined effects of stress and high temperature. This study used the UCG technique with strip mining, face mining, and gasifier-controlled retraction injection technology. The results indicate that arch height has a strong influence on pillar stress.

A literature review shows that the issues of surface subsidence and the stability of the pillars between reactors were usually studied separately. The works of Xu et al. [32] and Li et al. [33] bring the study of pillar stability closer to the real situation, when the pillar walls are not straight due to coal gasification. This is confirmed by field monitoring of the cavity forms presented in [11]. However, the aforementioned authors did not study the influence of pillar parameters or their stability on surface subsidence. Studies on surface subsidence above UCG cavities usually do not take into account the actual (non-rectangular) shape of these cavities and pillars. Moreover, the fact that a cavity in the form of a dome or arch is formed above the reactor—and that the cavity itself is filled with combustion products and collapsed roof rocks, as described in [11]—is also not taken into account. In addition, subsidence does not evolve instantly but rather develops over a fairly long time period (sometimes up to several years) after coal extraction. The temperature of the rock stabilizes during this time. Thus, thermal stresses primarily affect the stability of the roof and pillars, but do not directly affect surface subsidence. Therefore, it is advisable to carry out surface subsidence analysis step-by-step: at the time of gasification, thermal and mechanical stresses should be taken into account, and after coal gasification is completed, only mechanical stresses should be taken into account. The aforementioned issues constitute a research gap. The aim of this study is to investigate the influence of pillar width on surface subsidence, taking into account pillar shape and the presence of a cavity above the UCG reactor in the immediate roof.

The multifield finite element analysis performed using ANSYS software was used to study surface subsidence, the stress–strain state, and temperature distribution in the surrounding rock. The sizes of the heat-affected zones near the UCG reactor in the surrounding rock were determined. A reduction in the pillar's useful width due to coal gasification was established. The minimum required width of the pillar between the reactor cavities, which would prevent the negative impact of the gasification process on surface subsidence and overburden movement, was determined. This result makes it possible to increase the safety and reliability of the UCG process.

2. Engineering Background

2.1. Geological and Engineering Conditions

Ukraine has significant coal reserves, estimated at 120 billion tons, ranking first in Europe [34]. However, due to the Russian invasion, some of the coal mines in the territory controlled by the Ukrainian government were destroyed, and some stopped production due to air attacks, artillery shelling, and the destruction of coal-fired plants. The post-war reconstruction of the country will require significant energy resources.

The lack of significant oil and gas reserves, combined with the country's substantial coal reserves, determines the great potential of underground gasification. Destroyed infrastructure of Ukrainian coal mines and the global trend toward decarbonization have made this technology especially promising.

The Kotlyarevska mine was the research object of this study. This mine is located in the southwestern part of the Pokrovsk region, Donbas, Ukraine. Currently, coal production at the mine has been stopped due to the destruction of surface infrastructure. The mine's coal reserves are contained in two seams, l_1 and k_8. The reserves of the k_8 seam are almost depleted, while seam l_1 was being mined. The remaining reserves of the latter seam are estimated at 34.6 million tons of hard coal. It is expedient to consider this seam for the implementation of an underground gasification project. The mining and geological conditions of the mine are typical for the southern Donbas region. The thickness of the coal seam was 1.05–1.35 m and the dip angle varied from 11 to 13 degrees. The immediate roof strata of the coal seam in the studied area are weak mudstone, with a thickness of up to 3.0 m. The main roof is sandstone with the thicknesses of up to 30 m. The floor of the coal seam is represented by mudstone, with a thickness of 3.0 m, and sandy mudstone, with a thickness of up to 8.0 m. Underneath is massive sandstone (Figure 1a).

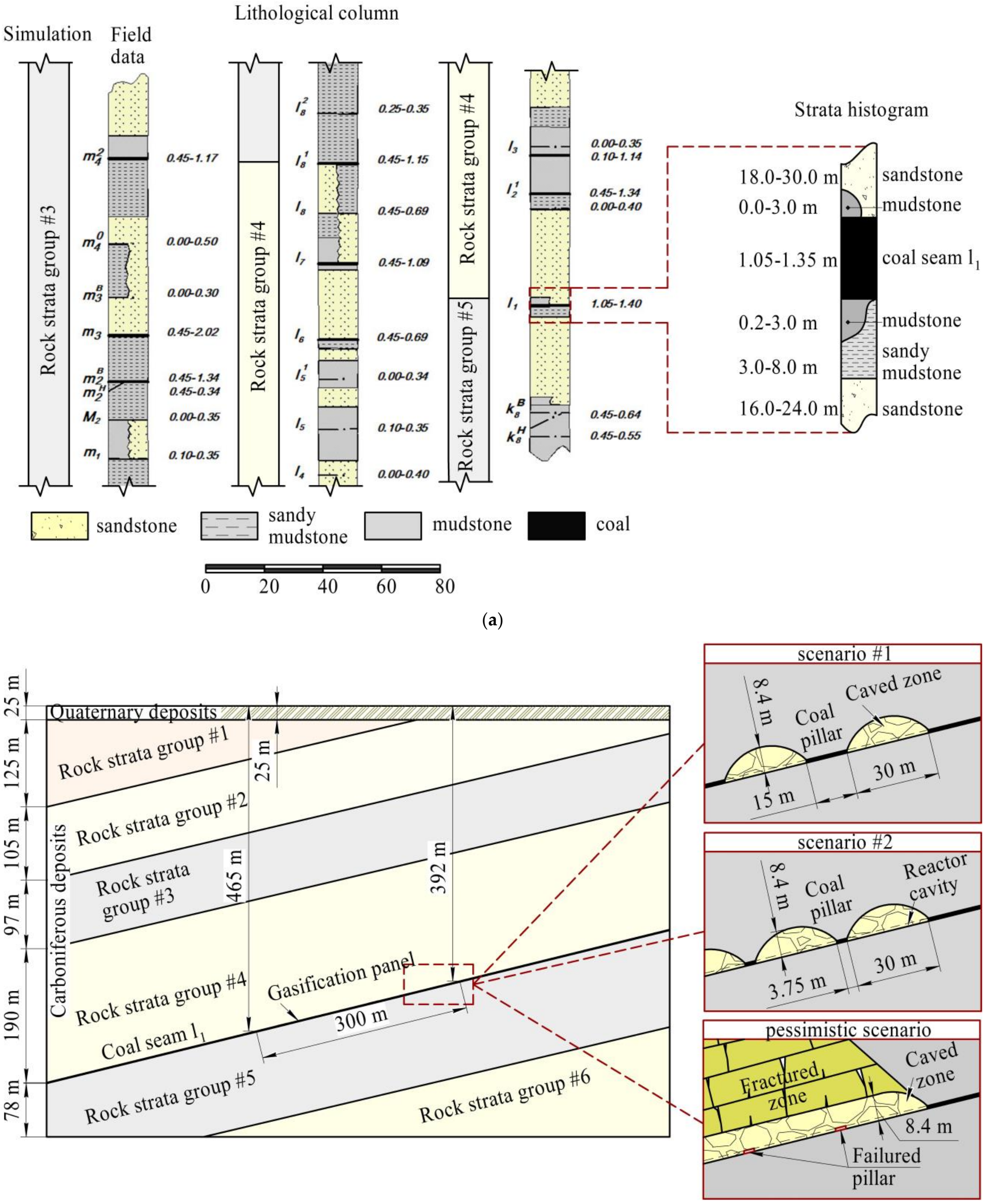

(**a**)

(**b**)

Figure 1. The geological and engineering conditions of gasification: (**a**) strata histogram; (**b**) vertical cross-section.

The rock mass in the mine field is characterized by Carboniferous rocks, represented by sedimentary deposits of sandstone, sandy mudstones, mudstones, limestones, and middle Carboniferous coal seams. The coal-bearing strata are represented mainly by layers of sandstone, sandy mudstones, and mudstones of different thicknesses. The average uniaxial compressive strength is as follows: sandstones—50–60 MPa, sandy mudstones—35–40 MPa, and mudstones—18–28 MPa. Figure 1a shows the lithological column of Carboniferous rocks. For the numerical simulation performed in this study, the lithological column was simplified, and the rock strata were combined into groups. The groups differed in the proportion of sandstones in the considered strata. Even visually, it is clear that in group 4, the proportion of sandstones is greater than in group 3. The inclusion criterion for the strata group was the average weighted compressive strength. If the strength of a rock lithotype differed by more than 20% from the average strength of the group, this lithotype was included in a new group. In this case, layers with a thickness of more than 1.0 m were taken into account. After that, the grouping process was repeated.

Carboniferous strata are found under the cover of Quaternary and Paleogene-Neogene deposits. Paleogene sediments are found on Carboniferous rocks with an angular unconformity, deposited by quartz sands, clays, and rocks, with lenses of ferruginous sandstones and quartzites. Neogene deposits are found in the form of islands in the western and southwestern parts of the Donbas. These are usually clays and sands. Quaternary sediments are represented by clays and loams with a thickness of 10–20 to 50 m, distributed almost everywhere.

The hydrogeological conditions in the mine field are favorable. Water inflows into the working faces during operation did not exceed 3 cubic meters per hour. There is no danger of water breakthrough from aquifers. Safety pillars are located near large geological faults, and coal gasification in such areas is not recommended. Therefore, the article does not take into account the influence of fault structures and other geological factors on the subsidence.

The part of the l_1 seam with a dip length of 300 m is adopted as a coal gasification panel. The upper boundary of this panel is located at a depth of 392 m, while the lower boundary is located at a depth of 465 m (Figure 1b).

This article examines three UCG scenarios. In scenario #1, the safety pillar width was 15 m, in scenario #2, it was 3.75 m (Figure 1b). In this way, the smallest and the largest values of the rational range of the pillar width were modeled [24–28]. In scenario #1, the gasification panel had seven cavities and six pillars (70% of coal extraction), while in scenario #2, it had nine cavities and eight pillars (90% of coal extraction). Both of these scenarios assume the sustained stability of the coal pillar. Also, a pessimistic scenario assuming the failure of safety pillars between the reactor cavities was simulated. In this case, the surface subsidence responses to the accident were studied.

2.2. Project Overview

The Parallel Controlled Retraction Injection Point (CRIP) method was employed in this research study (Figure 2). CRIPs are components used in UCG processes to inject air, oxygen, or steam into the reactor. The main goal of using the CRIP method in UCG is to facilitate the controlled conversion of coal into synthetic gas (syngas) underground, which can then be extracted for a variety of energy and industrial applications [35,36]. Linear CRIP involves a single injection well and a single production well. The produced gas is collected through the production well. Parallel CRIP involves multiple injection wells and multiple production wells. The injection wells are drilled parallel to the coal seam. The injection wells are then retracted at a controlled rate, and the coal is gasified as the combustion front moves upward [37]. The producer gas is collected through the production well (Figure 2). A comparison of the linear CRIP and parallel CRIP technologies by Seifi et al. [36] and Lozynskyi et al. [37] showed a higher efficiency of synthesis gas produced using parallel CRIP. In addition, the Parallel CRIP method is characterized by more stable gas production levels and increased coal utilization rates. This corresponds to the concept of a sustainable and efficient world energy system.

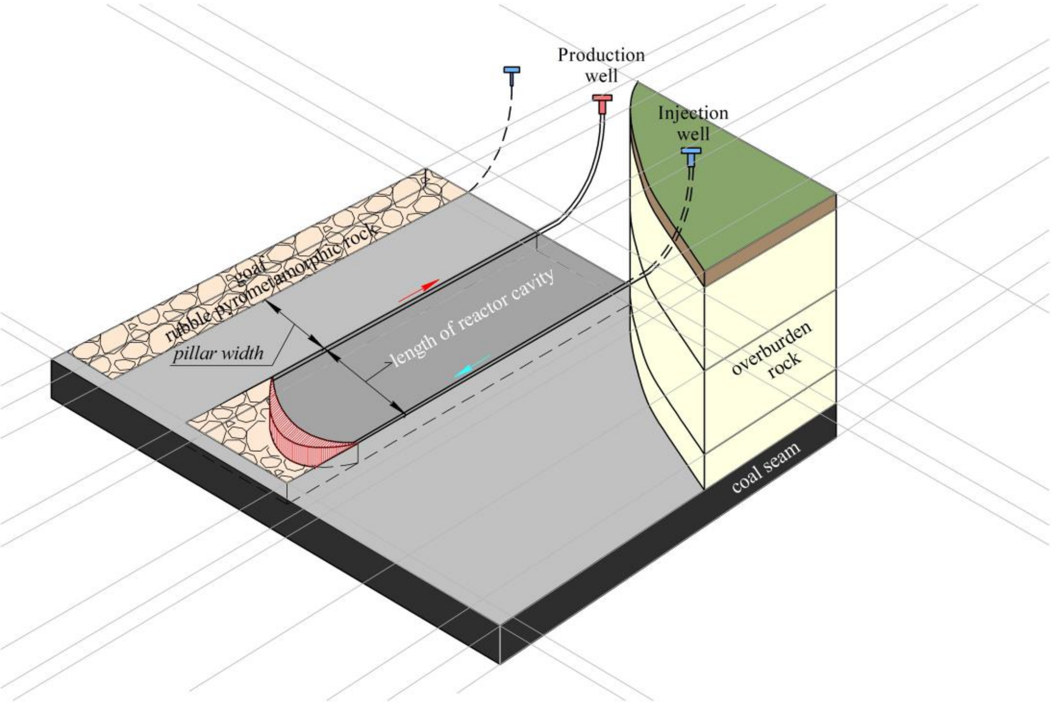

Figure 2. Parallel Controlled Retraction Injection Point (CRIP) method.

Multiple gasification cavities were investigated using parallel CRIP. The length of the reactor cavities was 30 m. The numerical simulation was carried out in two stages. At the first simulation stage, scenario #1, scenario #2 and pessimistic scenario were simulated. A caved zone in the form of an arch was modeled above the gasification cavity. The height of the caved zone was equal to 8.4 m, which is 8 times higher than the thickness of the coal seam [38,39]. The caved zone was filled with combustion products and collapsed roof rocks. The aim of the first simulation stage was to analyze the surface subsidence and rock mass movement above the gasification cavities for different pillar widths. Moreover, there was another aim: to analyze the surface subsidence and rock mass movement in the case of the failure of the safety pillars between the reactor cavities.

At the second simulation stage, the stability of the pillars was investigated to optimize the width of the safety pillars between the reactor cavities. The optimization criterion was minimal coal losses in the pillars. In this case, the hyperbolic shape of the pillars [32,33] and thermal stresses in the surrounding rocks from the gasification reactor were taken into account.

3. Study of Surface Subsidence and Rock Mass Movement Above the Gasification Cavities: Materials and Methods

3.1. Numerical Model at First Simulation Stage

The finite element method performed in ANSYS software was used for the study. The models were three-dimensional. At the first simulation stage, the model was 900 m wide, 620 m high, and 100 m long (Figure 3a). The lateral boundaries of the model were fixed against the corresponding horizontal displacements, and the bottom boundaries were fixed against the corresponding vertical displacements. The vertical gravity was set in the model.

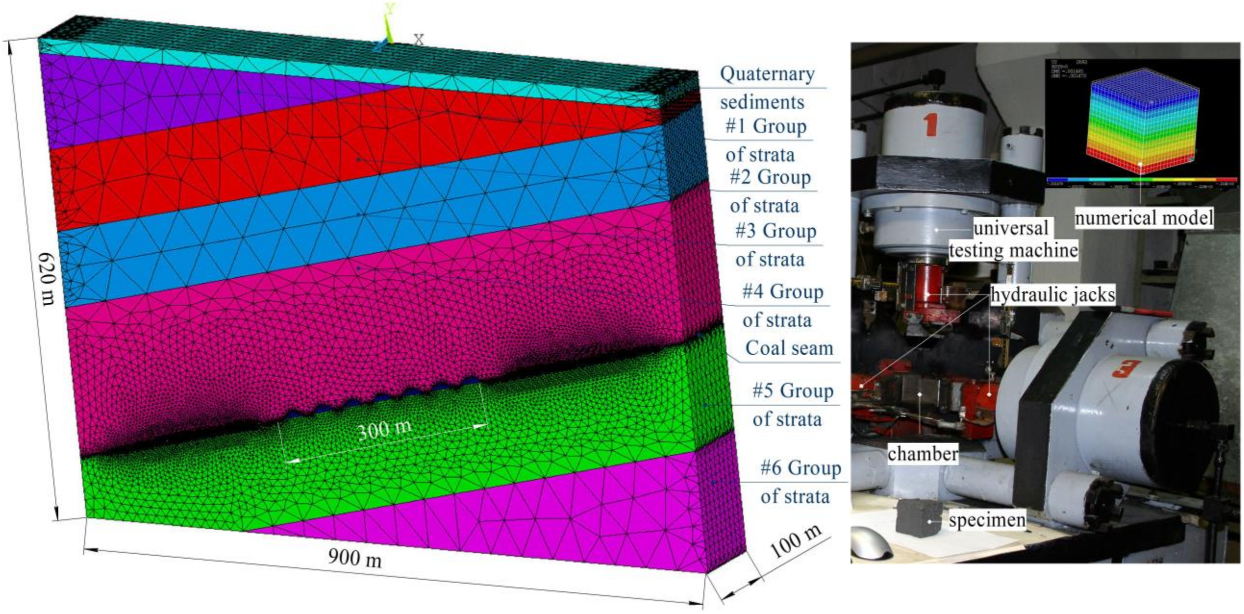

(**a**) (**b**)

Figure 3. (**a**) Numerical model at the first simulation stage (**b**) and laboratory tests of rock specimens for calibration of the numerical model.

To simulate the behavior of rocks, an orthotropic model was used. This model allows the simulation of the behavior of anisotropic materials, such as sedimentary rocks [40–43]. The variation in the physical and mechanical properties of rocks along and across the stratification was determined using the calibration numerical model proposed by Sakhno et al. [44]. The calibration results are generally concordant with the findings of Prof. Rzhevsky.

The initial rock properties were established by testing cube-shaped specimens under triaxial compression with unequal components (Figure 3b). The horizontal stresses were equal to 30% of the vertical stresses, which corresponded to the overburden stress field. The size of the specimen was 55 × 55 × 55 mm ± 0.1 mm. Based on the obtained stresses and deformations, the elastic moduli (E_1, E_2, E_3) and Poisson's ratios $(\nu_{12}, \nu_{23}, \nu_{31})$ were calculated in three mutually perpendicular directions. After this, the value of the moduli of shear elasticity (G_{12}, G_{23}, G_{31}) was calculated using the following formulas:

$$G_{12} = \frac{E_1}{2(1+\nu_{12})}, \text{ MPa} G_{23} = \frac{E_2}{2(1+\nu_{23})}, \text{ MPa} G_{31} = \frac{E_3}{2(1+\nu_{31})}, \text{ MPa} \tag{1}$$

After this, a calibration numerical model of the 55 × 55 × 55 mm specimen was created in ANSYS software; the properties E_1, E_2, E_3, ν_{12}, ν_{23}, ν_{31}, G_{12}, G_{23}, and G_{31} that were calculated based on the results of the laboratory test were assigned, and the model was loaded (Figure 3b). After this, the model was calibrated by an iterative method.

The properties of the rocks in the groups of strata were changed proportionally to the change in the average elastic modulus. Moreover, the values of Poisson's ratios were the same in all groups. The properties of rocks in the groups of strata are given in Table 1. To simulate the behavior of the collapsed roof rocks in the caved zone, Poisson's ratio ν = 0.45, and E = 30 MPa were applied [45].

Table 1. Rock mass material parameters for numerical simulation at the first simulation stage.

E_1, (GPa)	E_2, (GPa)	E_3, (GPa)	ν_{12}	ν_{23}	ν_{31}	G_{12}, (GPa)	G_{23}, (GPa)	G_{31}, (GPa)	Density, kg/m^3
Quaternary sediments									
1.5	6.5	1.5	0.27	0.1	0.25	0.59	2.95	0.60	2100
Rock strata group #1									
2.2	20.1	2.2	0.23	0.12	0.22	0.89	8.97	0.90	2450
Rock strata group #2									
2.9	23.8	2.9	0.23	0.12	0.22	1.18	10.63	1.19	2500
Rock strata group #3									
2.4	19	2.4	0.23	0.12	0.22	0.98	8.48	0.98	2500
Rock strata group #4									
2.7	22.7	2.7	0.23	0.12	0.22	1.10	10.13	1.11	2500
Rock strata group #5									
2.2	20.1	2.2	0.23	0.12	0.22	0.89	8.97	0.90	2500
Rock strata group #6									
2.4	19	2.4	0.23	0.12	0.22	0.98	8.48	0.98	2500

The simulation at the first stage was carried out step-by-step as follows.

Step 1 (prestress stage): Loading the model with gravity and writing the values of stresses and displacements in all nodes of the model to a file using the “Inistate” script in ANSYS Parametric Design Language.

Step 2 (initial stress-strain stage): Reading the recorded data from the file and recalculating the model for zeroing displacement. In this case, a situation of the initial stress-strain state of the strata was obtained.

Step 3 (post-gasification stage): Analyzing the stress-strain state of the model after coal gasification and the formation of caved zones.

The model was calibrated by comparing simulated subsidence in the pessimistic scenario with the monitoring data of the subsidence above the longwall. As mentioned above, the pessimistic scenario assumed the failure of the safety pillars between the cavities. In this case, after pillar failure, the immediate roof will also collapse along the length of the gasification panel. Above the goaf, a caved zone and a fractured zone will be formed, as happens above the longwall [38].

3.2. Simulation Results of the First Simulation Stage

3.2.1. Pessimistic Scenario

Figure 4 shows the evolution of vertical displacements in the model during the step-by-step simulation of surface subsidence and the movement of rock masses above the gasification panel. The vertical scale of displacement in Figure 4 is 1:20. According to the pessimistic scenario, all cavities within the panel have been worked out and the safety pillars have failed. Thus, the mechanisms of surface subsidence and the movement of rock masses are simplified to the same mechanisms as those above the longwall.

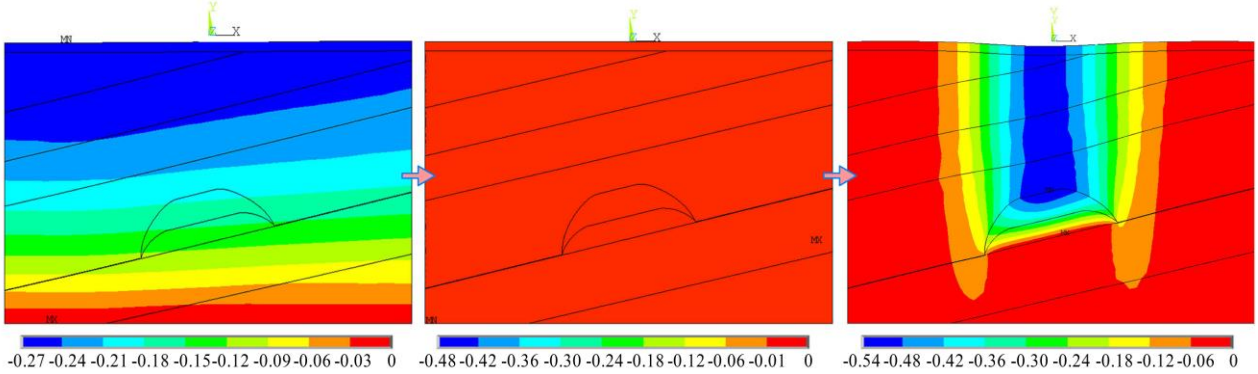

(**a**) (**b**) (**c**)

Figure 4. Vertical displacement (m) evolution in the sequence of simulation process for the pessimistic scenario: (**a**) Step 1 (prestress stage); (**b**) Step 2 (initial stress-strain stage); (**c**) Step 3 (post-gasification stage). MX is the maximum value of the parameter, MN is the minimum value of the parameter.

This model was used for the final calibration of the rock properties. For this purpose, the results of the calculation of surface subsidence in the model were compared with the results of subsidence monitoring over the southern longwall of the l_1 seam of the Kotlyarevska mine. The basic regularities of the subsidence are sufficiently well-studied, and they are the basis for the relevant normative documents that take into account regional characteristics. For the conditions of the Ukrainian Donbas, the parameters of the subsidence are calculated in accordance with the DSTU 101.00159226.001-2003 "Rules of undermining Earth surface objects". This makes it is possible to calculate subsidence outside fault zones and aquifers, taking into account the error of measuring instruments with an accuracy of up to 5%. The procedure is also described in a previous study [38]. The corresponding surface subsidence graphs are shown in Figure 5. As can be seen in Figure 5, after calibration of the numerical model, the graph of the surface subsidence curve is close to the subsidence curve obtained during monitoring.

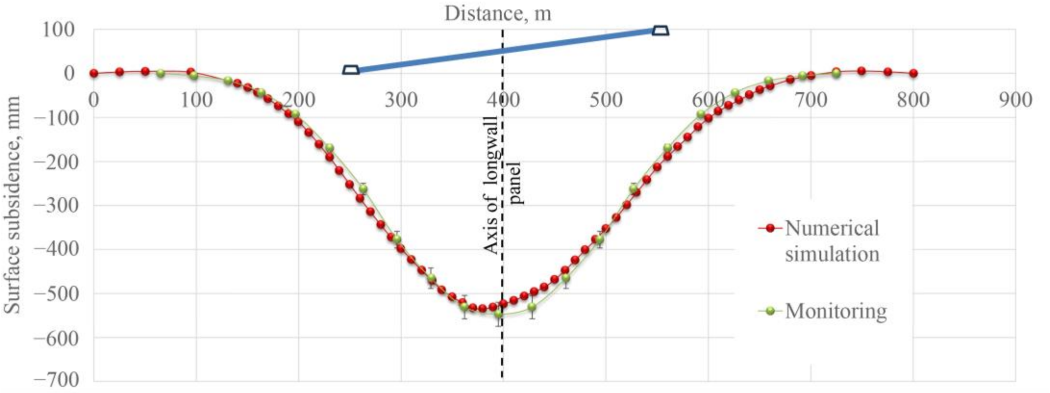

Figure 5. Surface subsidence according to simulation and monitoring results (pessimistic scenario).

The maximum vertical displacement in the numerical model is 543 mm, and according to the monitoring results, it is 550 mm. The width of the subsidence trough in the numerical model is 660 m, and according to the monitoring results, it is 630 m.

The accuracy of the numerical model was assessed on the basis of error measures. Percent error for maximum subsidence is as follows:

$$\mu_{smax} = \frac{S_{max}^{mon} - S_{max}^{sim}}{S_{max}^{mon}} 100\% \mu_{smax} = \frac{550 - 543}{550} 100\% = 1.27\% \quad (2)$$

where S_{max}^{mon} is the maximum value of monitored subsidence, mm and S_{max}^{sim} is the maximum value of simulated subsidence, mm.

Percent error for width of the subsidence trough is as follows:

$$\mu_{bmax} = \frac{B^{mon} - B^{sim}}{B^{mon}}100\%\mu_{smax} = \frac{660 - 630}{660}100\% = 4.72\% \tag{3}$$

where B^{mon} is the width of the subsidence trough according to the monitoring results, m and B^{sim} is the wid of the First Simulation Stage th of the subsidence trough according to simulation results, m.

The obtained error measures show the sufficient accuracy of the model.

Vertical and horizontal displacements of rock masses at depths of 100, 200, and 300 m, as well as on the surface, in the pessimistic scenario are shown in Figure 6.

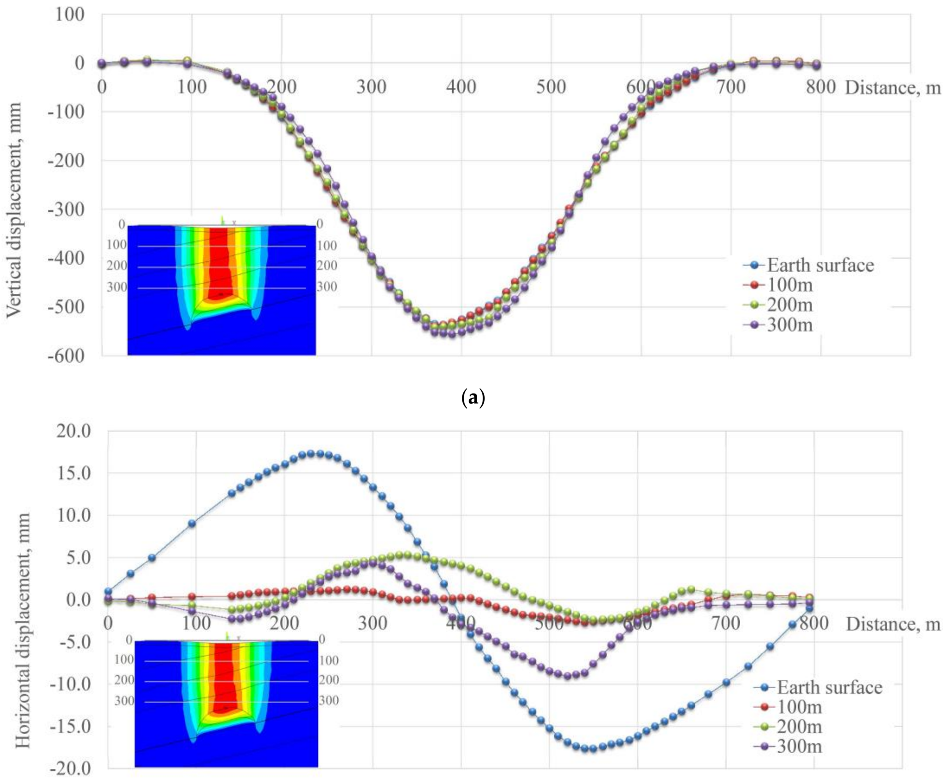

(**a**)

(**b**)

Figure 6. Vertical (**a**) and horizontal (**b**) displacements of rock masses and earth surface in the pessimistic scenario.

Analysis of the vertical displacements (Figure 6a) indicates a tendency to increase insignificantly with depth. Thus, surface subsidence, vertical displacement at a depth of 100 m, and at depth of 300 m are equal to 536, 538 mm, and 555 mm, respectively. The width of the subsidence zone in the depth range of 0–300 m does not change significantly. A noticeable increase in the width of the zone of the goaf's influence is observed at a height of up to 100 m above the gasification panel. The brittle sandstones lie in the rock strata among other rocks; therefore, the failure of these sandstones is inevitable when taking into account the aforementioned displacements.

Horizontal displacements (Figure 6b) have a general tendency to decrease from the surface to the depth. Thus, on the surface, the maximum horizontal displacement is 17.3 mm, and at a depth of 300 m it is 9 mm. However, between the depths of 100 and 300 m, horizontal displacements increase. In addition, unlike vertical subsidence, a clear asymmetry of horizontal displacement is observed, which is explained by the non-horizontal dip angle and the intersections of the receiving data line (highlighted in grey in Figures 5 and 6) with the contact surface of the strata. Thus, horizontal displacements can be used to track the movement of the axis of the zone of gasification influence with depth. This axis shifts first to the right (along the uphill of the strata at a depth of 100–200 m) and then to the left (along the downhill of the strata, at a depth of 200–300 m). Horizontal displacements confirm the high probability of crack initiation and rock failures.

Analysis of the simulation results shows that surface subsidence and rock displacement exceed the peak values for the non-destructive bending of rock layers. This indicates a high risk of discontinuity of the overburden rock, crack initiation above the gasification panel, a change in the groundwater regime, and high water inflow into the gasification cavities. Thus, the failure of the pillars between reactor cavities is a threat to surface infrastructure and to the stability of the groundwater regime. Therefore, special attention should be paid to the clarification of safety pillar parameters when designing UCG methods.

3.2.2. Scenario #1 and Scenario #2

Figure 7 shows the vertical displacements in the model above the gasification panel in scenario #1 and scenario #2. The vertical scale of displacement in Figure 7 is 1:20. The points of maximum vertical displacement are located in the central part of the gasification panel. Graphs of the vertical and horizontal displacements of the surface and rock mass at depths of 100, 200, and 300 m are shown in Figure 8. Analysis of these graphs shows that the associated rock movements are insignificant. Surface subsidence does not exceed 27 mm in scenario #1 or 46 mm in scenario #2. As in the pessimistic scenario, vertical displacement increases insignificantly with depth (Figure 8a,c). However, the magnitude of surface subsidence according to scenario #1 is 11.7 times less, while according to scenario #2 it is 19.9 times less than in the pessimistic scenario. The width of the trough, despite the smaller subsidence magnitude, does not differ from the width of the trough in the pessimistic scenario.

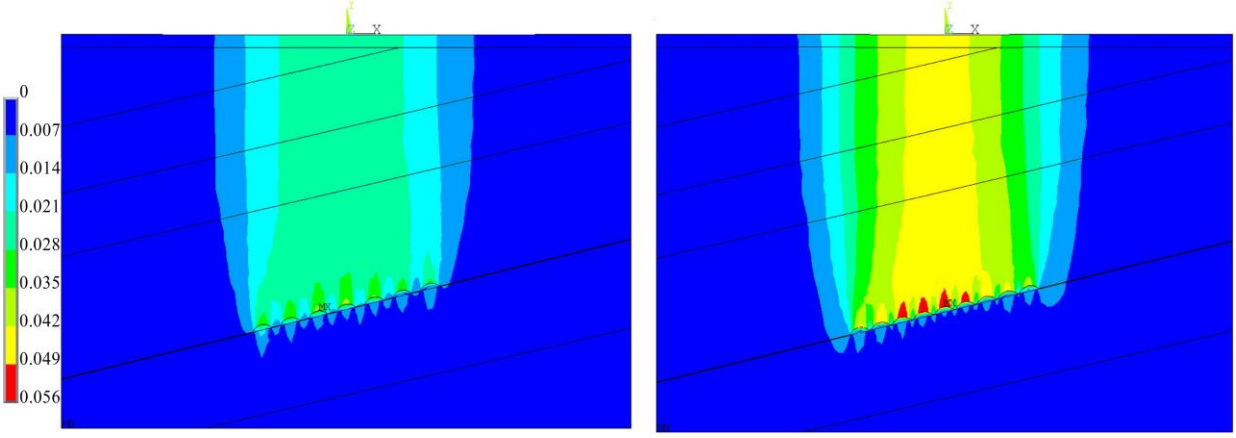

(a) (b)

Figure 7. Vertical displacement (m) distribution: (**a**) scenario #1; (**b**) scenario #2. Vertical displacement exaggeration 20:1.

Horizontal displacements on the surface are 9.6 times smaller in scenario #1 and 16.3 times smaller in scenario #2. Horizontal displacements of the surface are higher than those at depth. Unlike the pessimistic scenario, here there is no tendency for horizontal displacements to increase with depth. In both scenario #1 and scenario #2, horizontal displacements at a depth of 100 m are close to zero, then increase insignificantly at a depth of 200 m, and decrease again at a depth of 300 m. The displacement axis shifts to the right (along the uphill of the strata at a depth of 100–200 m) and then returns to its initial position at a depth of 200–300 m. Horizontal displacements confirm the low probability of crack initiation in the rock mass and on the surface.

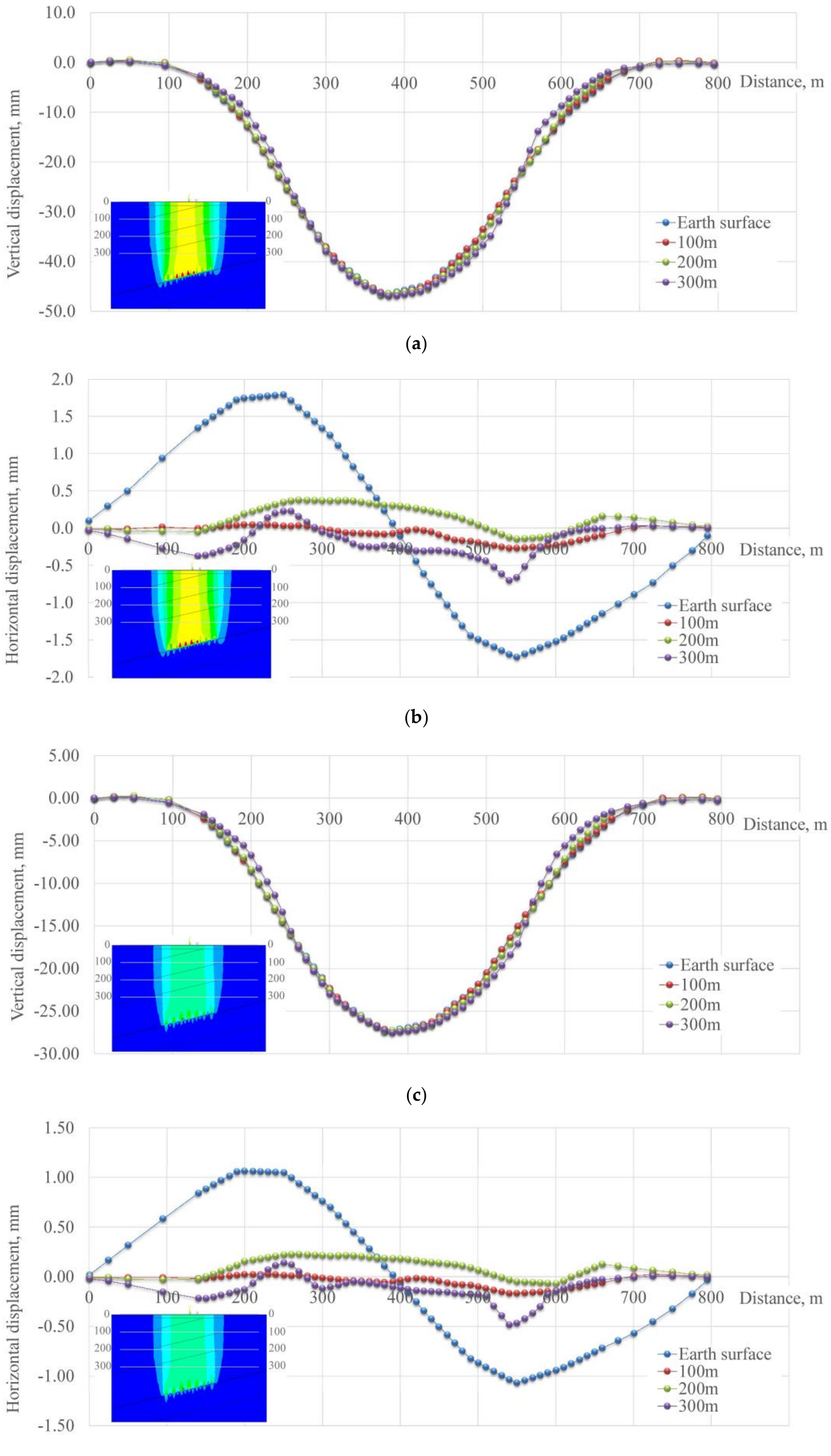

(a)

(b)

(c)

(d)

Figure 8. Vertical and horizontal displacements of rock mass and earth surface in scenario #1 (**a**,**b**) and scenario #2 (**c**,**d**).

The most intense movements are not located beyond the boundaries of the main roof (Figure 7). This is also confirmed by the analysis of minimum principal stress distribution (Figure 9). If the stresses in the pillars at the boundaries of the gasification panel are not taken into account, the failure of the rock masses and the surface in both the first and second scenarios is improbable because the stresses that are formed in the rocks are significantly lower than their ultimate strength. The stresses at 70 m above the gasification panel do not differ from the stresses in the rock mass outside the zone of gasification influence.

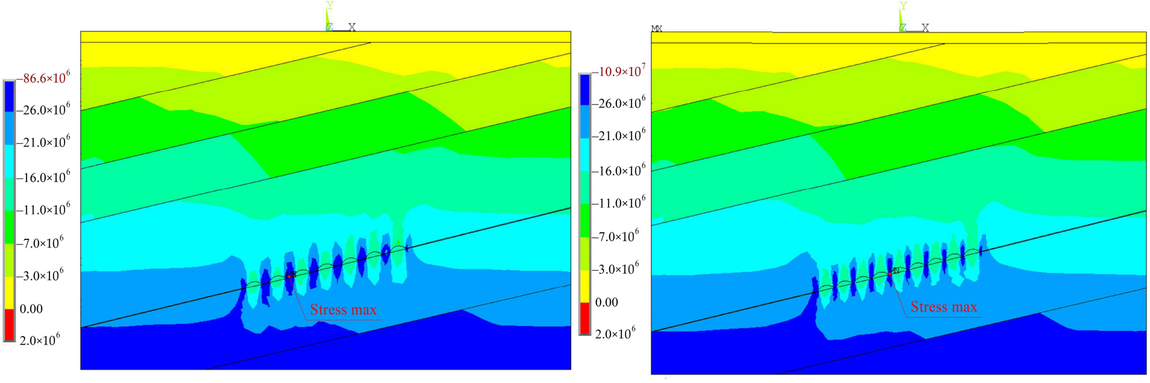

(**a**) (**b**)

Figure 9. Minimum principal stress (Pa) distribution: (**a**) scenario #1; (**b**) scenario #2. Negative stress values indicate compression.

As for the stresses in the pillars, their maximum is located in the central part of the gasification panel (indicated in Figure 9). According to the first simulation stage, in both the first and second scenarios, the stresses exceed the ultimate strength of the rocks. According to scenario #1, the maximum compressive stresses are 86.6 MPa, and according to scenario #2 they are 109 MPa. However, point estimates are not sufficient to draw conclusions about the stability of the pillars, so this issue requires more detailed investigation. Such a study was carried out at the second stage of numerical simulation.

3.3. Simulation Discussion of the First Simulation Stage

Several conclusions can be drawn from the above analyses:

(1) During underground gasification of a thin coal seam (with a thickness of 1.05 m)—at a depth of 392–465 m and using the CRIP method, with a length of the reactor cavities of 30 m for both scenario #1 and scenario #2—surface subsidence and rock movement are insignificant. The most intense movements are located above the gasification cavity, within the boundaries of the main roof. Analysis of vertical and horizontal displacements shows the low probability of crack initiation in the rock mass and on the surface. However, a prerequisite for this is the stability of the pillars between the gasification cavities.

(2) In the case of the failure of the pillars between the gasification cavities (pessimistic scenario), there is a high probability of crack initiation and overburden rock failures. Analysis of vertical and horizontal displacements shows that, in this case, surface subsidence and rock displacement exceed the peak values for the non-destructive bending of rock strata. The surface infrastructure is therefore at risk of destruction. As a result of the crack growth above the gasification panel, the destruction of water-bearing sandstones and water breakthroughs into the gasification cavities are possible.

(3) According to the first simulation stage, the maximum compressive stresses in the pillars are located in the central part of the gasification panel. In this case, the principal stresses exceed the ultimate strength of the rocks. However, the estimation of the pillars' stability should be carried out more thoroughly and on a larger scale, taking into account all the adequate assumptions. Such an investigation was carried out at the second stage of numerical simulation.

4. Analysis of Safety Pillar Stability

4.1. Numerical Model at the Second Simulation Stage

The Drucker–Prager model implemented in ANSYS code was used to simulate the behavior of rock mass at the second simulation stage. The model was 100 m wide, 130 m high, and 50 m long (Figure 10). The model included two cavities at the post-gasification stage (with extracted coal) and one cavity at the gasification stage. The cavities located in the middle of the gasification panel were modeled because the stresses there, according to the results of the first simulation stage, were the highest. In this approach, the influence of boundary effects is neutralized. The model had a cutout on the front part, which made it possible to analyze the stress variations in 3D.

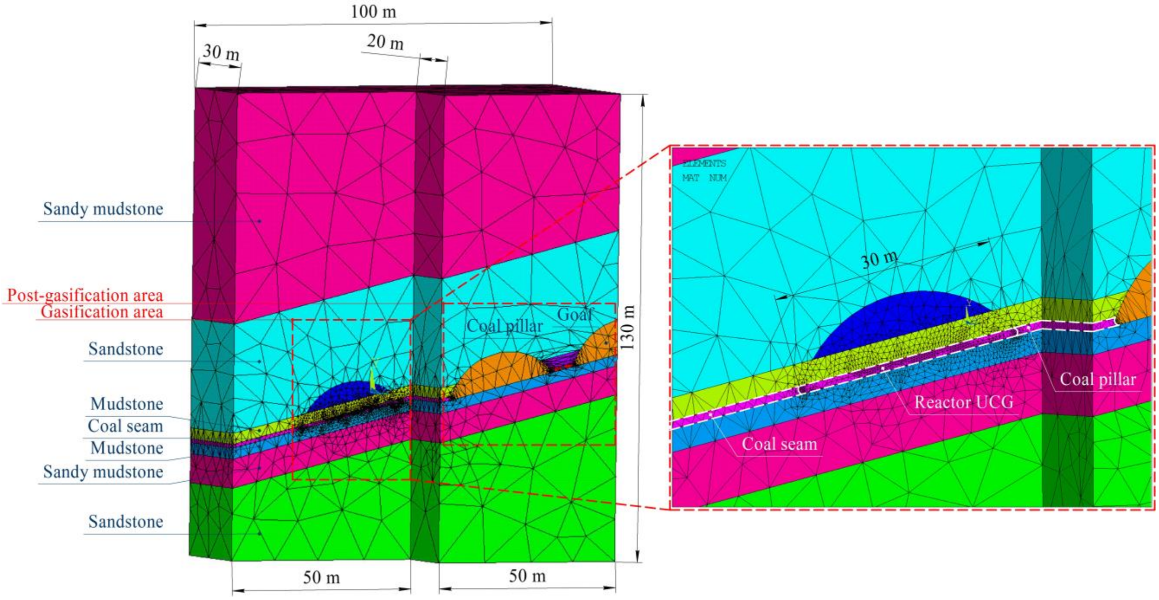

Figure 10. Numerical model at the second simulation stage.

The lateral boundaries of the model were fixed against the horizontal displacements in the direction perpendicular to the corresponding boundaries. The bottom boundary was fixed against the vertical displacements. Vertical pressure, which simulated overburden stress, was equivalent to the strata weight at a depth of 350 m (8.75 MPa). This pressure was applied to the top boundary of the model.

At the second simulation stage, five schemes were modeled. The schemes' difference was in the width of the safety pillars. At the same time, all the schemes had a constant gasification panel size (300 m) and cavity reactor size (30 m). Table 2 shows the parameters of the schemes.

Table 2. The parameters of the schemes for numerical simulation at the second simulation stage.

Scheme	Length of Gasification Panel (m)	Length of Reactor Cavity (m)	Number of Reactor Cavities	Width of Safety Pillar (m)	Number of Safety Pillars
I	300	30	5	37.5	4
II	300	30	6	24	5
III	300	30	7	15	6
IV	300	30	8	8.5	7
V	300	30	9	3.75	8

The Hoek–Brown Failure Criterion [46] was used to calculate the properties of rock mass outside the zone of gasification thermal influence. The GSI was calculated as RMR89-5 [47]. RMR89 was determined on the basis of geological documentation and the results of the uniaxial strength tests according to the Bieniawski method [48]. The "mi" constant was 8 for mudstones, 17 for coal, and 12 for sandstone. The D parameter corresponded to Hoek's classification categories [46]. The deformation modulus (E), friction angle (φ), and cohesive strength (c) were calculated according to Hoek and Diederichs' empirical method [47]. The calculation procedure was described in a previous study [49]. The calculated rock mass properties are presented in Table 3.

Table 3. Rock mass material parameters for numerical simulation at the second simulation stage outside the zone of thermal influence.

GSI	D	Deformation Modulus (GPa)	Poisson's Ratio	Cohesion Value, (MPa)	Angle of Internal Friction (deg)	Dilatancy Angle (deg)
Main roof (sandy mudstone)						
52	0.5	1.19	0.3	2.83	24	24
Main roof (sandstone)						
55	0.5	1.80	0.3	3.90	34	34
Immediate roof (mudstone)						
52	0.5	0.50	0.3	1.61	22	22
Coal seam						
35	0	0.22	0.3	1.13	20	20
Immediate floor (mudstone)						
47	0.5	0.50	0.3	1.61	22	22
Main floor (sandstone)						
55	0.5	1.80	0.3	3.90	34	34
Goaf (rubble pyrometamorphic rock)						
		0.06	0.45	-	-	-

The initial temperature of the rocks was 30 °C. The thermal impact in the model was applied at the reactor area, thereby simulating coal combustion. The temperature in the reactor was 1000 °C. Mechanical rock properties are generally highly dependent on temperature [16,50–53]. Therefore, rock properties must be simulated as temperature-dependent. However, studies by Otto and Kempka [54] show that the effect of considering temperature-dependent parameters is insignificant for the resulting temperature distribution. Therefore, in this study, temperature-independent rock mass properties were used.

A study of the change in the properties of rocks at high temperatures by Zhang et al. [55] showed that when mudstones are heated from room temperature to 400 °C, the elastic modulus increases by 60%, that when heated to 500 °C, it decreases to a magnitude similar to room temperature, and that after heating to 800 °C, it decreases by 65%. In this case, the uniaxial compression strength increases by 2.7 times when heated to 400 °C, and upon subsequent heating to 1000 °C, it decreases to a magnitude typical for room temperature [55]. Studies by Wu et al. [56], Sygała et al. [57], and Otto and Kempka [54] have shown that the Young's modulus of sandstone heated to 1000 °C decreases by an average of 58%, while its strength decreases slightly, by 5–7%. Taking into account these previous studies [54–57], the properties of the roof and floor rocks in the thermal impact zone of the UCG reactor were calculated (Table 4). Since the stability of the pillars and overburden rocks was investigated in this article, the mechanical properties of floor rocks in the zone of thermal influence were not changed. The thermal properties of the floor mudstones were the same as the thermal properties of the roof mudstones. The heat-affected zone was located near the reactor cavity in the surrounding rocks, as established by previous studies by Otto and Kempka [54], Wang et al. [58], Xin et al. [59], and Sarhosis et al. [60], and is also evident from the temperature distribution seen in the model shown in Figure 11a.

Table 4. Rock mass material parameters for numerical simulation at the second simulation stage within the zone of thermal influence.

Linear Thermal Expansion Coefficient (α) (K^{-1})	**Specific Heat Capacity (*CP*) (J/kg K)**	**Thermal Conductivity (λ) ($W \cdot m^{-1} \cdot K^{-1}$)**	**Tensile Strength (MPa)**	**Deformation Modulus (GPa)**	**Poisson's Ratio**	**Cohesion Value, (MPa)**	**Angle of Internal Friction (deg)**
			Main roof (sandstone)				
1.6×10^{-5}	1363	2.3	1.2	2.45	0.3	6.5	32
			Immediate roof (mudstone)				
1.0×10^{-5}	1363	1.67	0.36	1.17	0.3	2.7	27
			Coal seam				
5×10^{-6}	2000	0.23	0.27	0.5	0.4	1.13	20

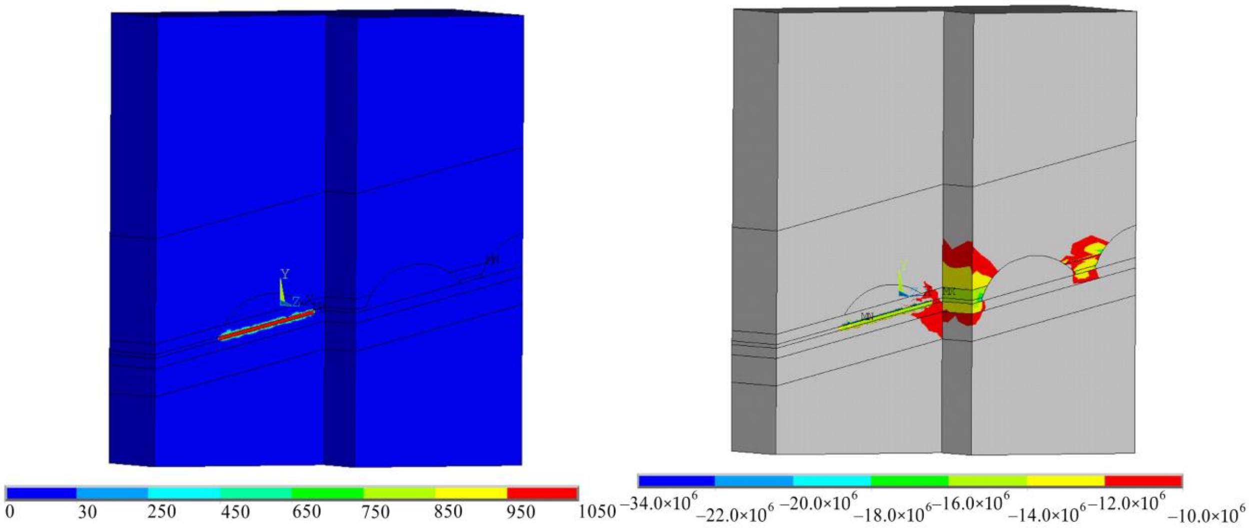

(**a**) (**b**)

Figure 11. Temperature (°C) of rock mass (**a**) and minimum principal stress (Pa) (**b**) distributions.

4.2. Simulation Results of the Second Simulation Stage

4.2.1. Stress Analysis in the Heat-Affected Zone of the UCG Reactor

Figure 11a shows the temperature distribution in the model. The blue color shows the rock mass temperature in the range of 0–30 °C. The heat-affected zones of the UCG reactor differs in color. The distribution of minimum principal stresses is shown in Figure 11b. Stresses with a minus sign are compressive. The thermal expansion of rocks in the influence zone of the UCG reactor causes an increase in stresses in the roof and floor, as well as in the coal pillar. The initial stress field is highlighted in gray in Figure 11b. High stress zones are highlighted in other colors. Thermal stresses are located in the immediate vicinity of the UCG reactor.

The distributions of rock mass temperature, minimum principal stress, and minimum principal strain in the thermally affected zone of the cavity reactor are shown in Figure 12. Figure 12a shows that the increase of rock mass temperature near the reactor occurs in an insignificant area of the surrounding rocks. Therefore, the zones of high stress and strain are also insignificant (Figure 12b,c). To refine the sizes of these zones, the finite element mesh near the cavity reactor was manually refined. The high stress in the pillar at the boundary with the reactor cavity exceeds 68% of the initial overburden stress. The minimum principal strains in the coal pillar do not exceed the elastic limit.

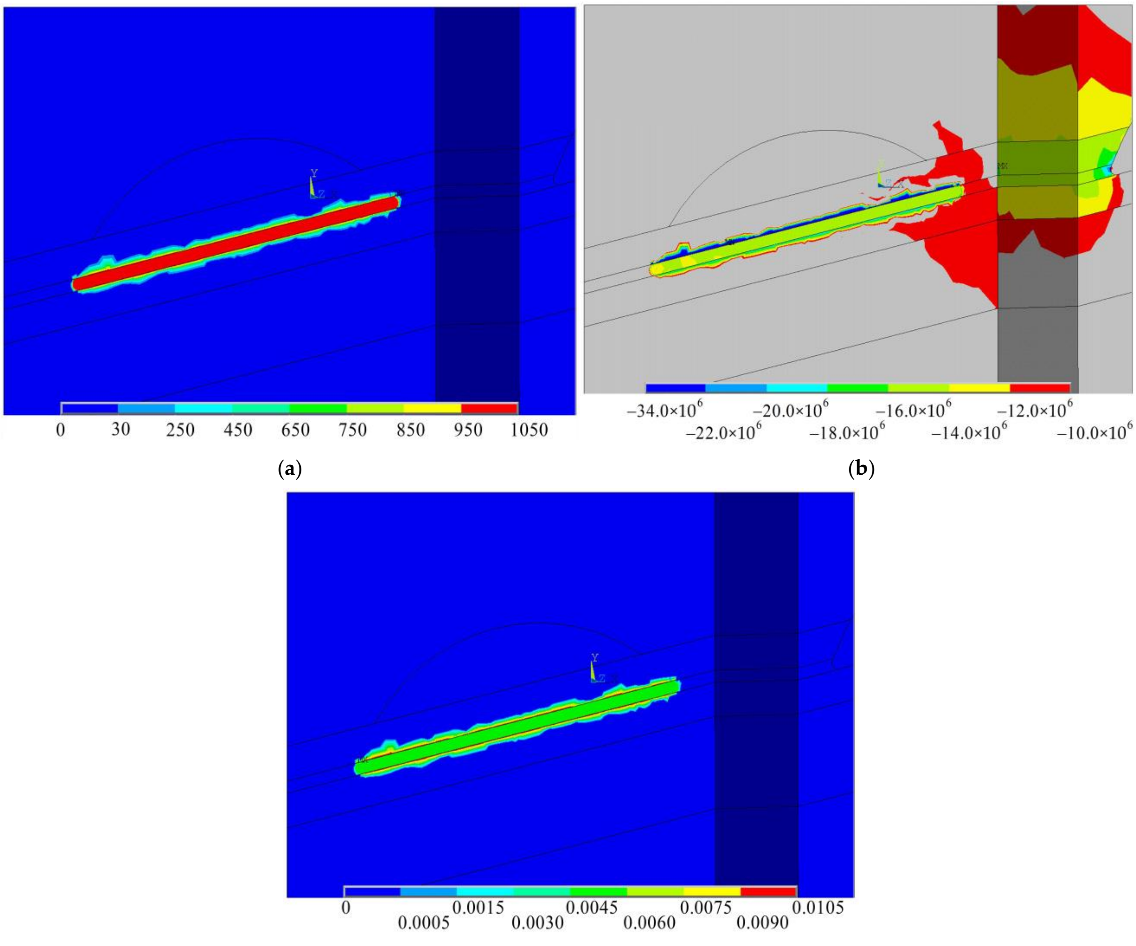

(**a**) (**b**)

(**c**)

Figure 12. The distribution of rock mass temperature (°C) (**a**), minimum principal stress (Pa) (**b**), and minimum principal strain (**c**).

To analyze the size of the heat-affected zone of the UCG reactor, graphs of the stress variations around the reactor cavity were created. Stress data analysis was performed along four monitoring lines (Figure 13a). Three monitoring lines were placed perpendicular to the bedding of rocks at the roof and were drawn in the center of the cavity reactor (line A-A^1), at the edge of the cavity reactor on the pillar side (line C-C^1) and between the two previous monitoring lines (line B-B^1). One monitoring line (D-D^1) was oriented parallel to the bedding of the rocks and was drawn in the center of the coal seam.

Figure 13a shows that the increase in stresses caused by the thermal expansion of the rocks is limited to a height of 0.63–0.75 m in the roof of the coal seam, and to a depth of 0.6–0.7 m in the floor. Beyond this zone in the roof, the rocks are in the stress relief zone at a height of up to 1.2–1.5 m. Above the relief zone, the stresses in the rock mass stabilize to overburden stress. Thermal stresses in the roof at the contour of the reactor cavity are higher than the overburden stress by 130% along the A-A^1 line, and by 143% along the B-B^1 line. Previous studies [54,58] show that the strength of mudstones, heated to a temperature of 1000 °C ($\sigma_{T=1000}$), decreases to 40% of the intact rock strength (σ_0). Thus, the ultimate strength of mudstone in the roof is as follows:

$$\sigma_{T=1000} = 0.4 \cdot \sigma_0 = 0.4 \cdot 27 = 10.8 \text{ MPa} \quad (4)$$

In the simulation, pillar failure is identified using the stress threshold criteria. In Figure 13a, the dashed red line shows a compressive strength limit of 10.8 MPa. The thermal stresses exceed the ultimate strength of rocks in the heat-affected zone (Figure 13a). Thus, the emergence and evolution of cavity zones in the roof of the coal seam begin at the gasification stage.

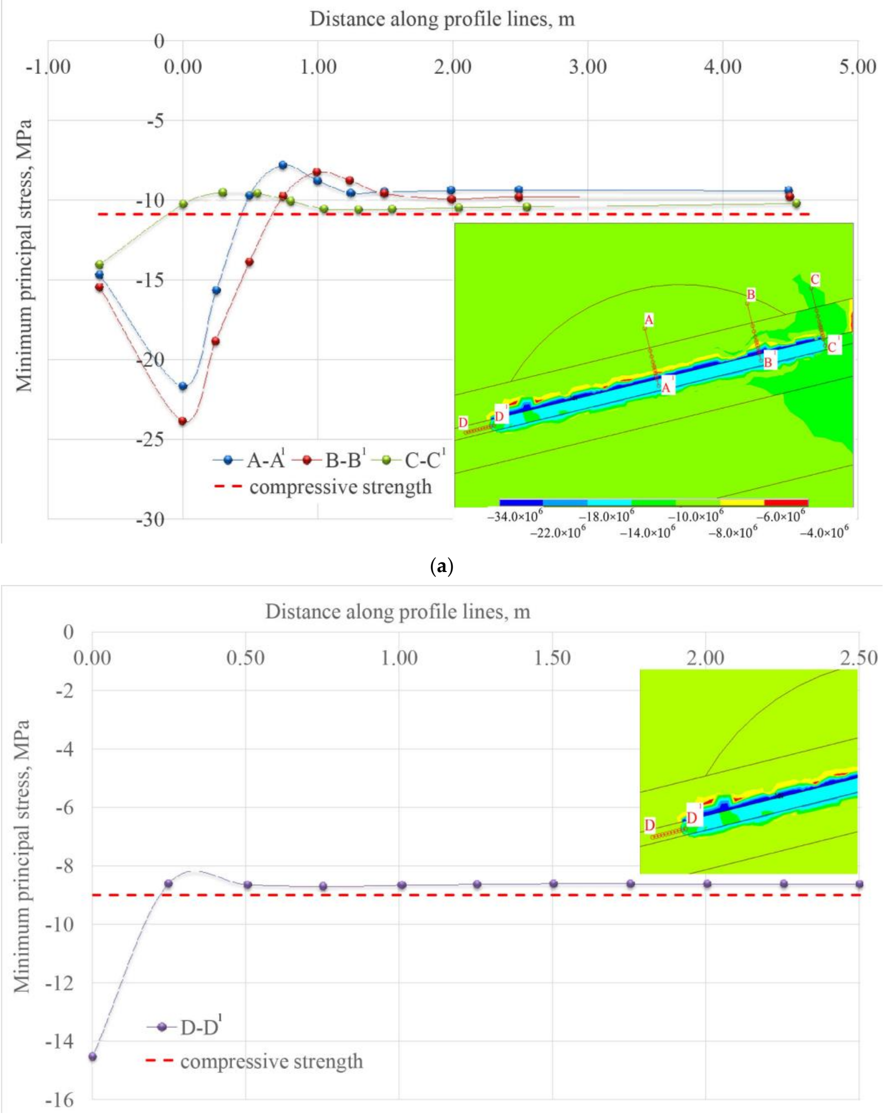

(**a**)

(**b**)

Figure 13. Minimum principal stress in the roof along the monitoring lines A-A^1, B-B^1, and C-C^1 (**a**) and in the coal seam along the monitoring line D-D^1 (**b**).

The stress field of rock masses around the edge of the reactor cavity on the coal pillar side (line C-C^1) differs from that described above. Thus, an increase in stresses in the roof at the contact point with the coal seam, characteristic of lines B-B^1 and A-A^1, is not observed along line C-C^1. On the contrary, the minimum principal stress is lower than the overburden stress. Previously conducted coal gasification in the adjacent cavity and the formation of caving zones led to stress relief. This has a positive effect on the stability of the rocks. The width of the low-stress zone in the side of the pillar is approximately 6.5 m (Figures 12b and 13a).

The zone of increased stress in the coal seam extends to a depth of 0.25 m (Figure 13b). The strength of the coal in the heating zone decreases, according to [54,61]. However, studies of coal strength under uniaxial compression at a temperature of 1000 °C have not been reported in the literature. Therefore, in this article, it was accepted that the compressive strength of coal decreases proportionally to a decrease in its tensile strength; for example, at 1000 °C, it decreases by 65–68%, according to [54,61]. Thus, it can be concluded that the tensile strength of the coal in the heat-affected zone will be 6.4 MPa for 650–1000 °C, 4 MPa for 600 °C, 1.6 MPa for 400 °C, and 9 MPa for 200 °C. Essentially, this means that the heating zone of coal determines its destruction zone. According to the simulation results, the depth of the heat-affected zone is 0.25 m (Figure 12a). In Figure 13b, the dashed red line shows the strength limit of the coal at −9 MPa, which is typical for a temperature of 200 °C. That is, with a pessimistic estimate, the depth of coal failure will be 0.25 m. Thus, at the gasification stage, there is a high risk of failure of the coal seam close to the UCG reactor. This can actually be interpreted as a reduction in the coal pillar width, which is important in the case of calculating pillar stability in the post-gasification period. For the conditions considered in the article, the useful width of the pillar is reduced by 0.5 m (since the depth of the failure zone is 0.25 m on each side).

4.2.2. Stress Analysis Outside the Heat-Affected Zone of the UCG Reactor

The distribution of minimum principal stresses in the surrounding rock in the case of a 3.75 m pillar width is shown in Figure 14a. Overburden stress at a depth of 350 m is 8.75 MPa. The gray color in Figure 14 shows minimum principal stresses lower than −10 MPa. High stress zones are highlighted in other colors. The highest stresses are located in the pillar. The zone of increased stress is shifted along the uplift, and includes rocks of the immediate and main roof. Increased stresses with a magnitude higher than 10 MPa extend up to 9 m into the roof of the coal seam and up to 3 m into the floor. Compressive stresses in the roof and floor are lower than their compressive strength; this indicates a low risk of rock failure. At the same time, the stresses in the pillar exceed the compressive strength of the coal, indicating a high risk of coal pillar failure. The highest stresses in the pillar are localized in its edge parts, which corresponds to the general idea of stress distribution in the pillars [62,63]. In the central part of the pillar, the stresses are reduced.

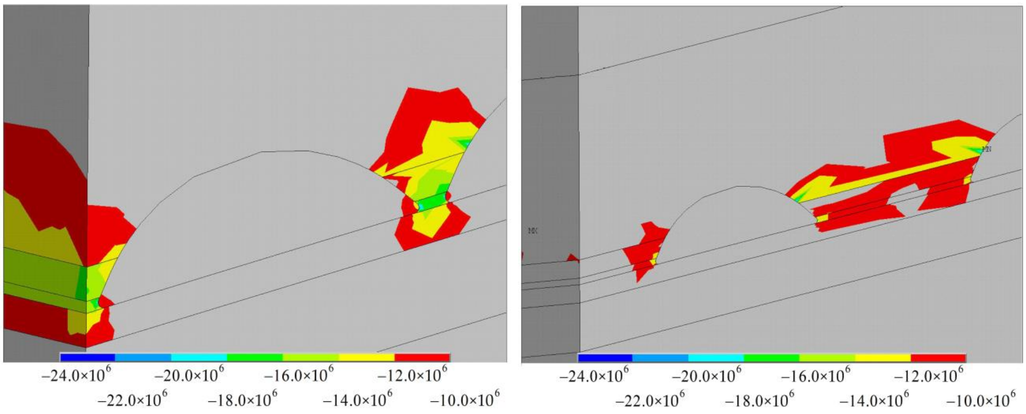

(**a**) (**b**)

Figure 14. The distribution of minimum principal stress in surrounding rock with a pillar width of 3.75 m (**a**) and 37.5 m (**b**). Negative stress values indicate compression. MX is the maximum value of the parameter, MN is the minimum value of the parameter.

Similar stress distribution is typical for other pillar sizes. Figure 14b shows the distribution of minimum principal stresses in the surrounding rock in the case of a 37.5 m pillar width. The stress magnitude in the pillar is noticeably lower, but the height and depth of the area of increased stresses in the roof and floor have changed insignificantly. The stress magnitude in the immediate roof also decreases with an increase in pillar width. But in the main roof, there is no obvious tendency to decrease the size of the increased stress zone and their magnitude. The minimum principal stresses in the pillar are lower than the compressive strength of the coal, which indicates a low risk of failure of the coal pillar.

Graphs of the stress variations in the coal pillars were created to optimize the safety pillar width. Stress data analysis was performed along monitoring line E-E^1, oriented parallel to the bedding of the rocks and drawn in the center of the coal pillar (Figure 15). The width of the safety pillar, according to the experiment plan (Table 2), varied from 3.75 to 37.5 m. The variations in minimum principal stress in coal pillars with a pillar width of 3.75–24 m have similar characteristics:

- Stress relief is observed at the edge of the pillar, which indicates the post-elastic stage of coal deformation;
- Beyond the relief zone, the highest stresses are concentrated near the edge of the pillar;
- The stress in the pillar gradually decreases to its center.

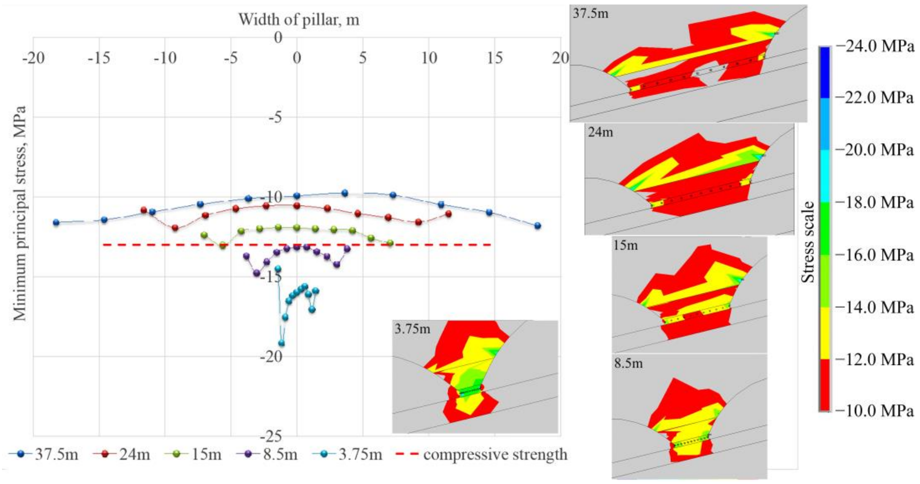

Figure 15. Minimum principal stress (MPa) in the coal pillar along the monitoring line E-E^1. Negative stress values indicate compression.

With a pillar width of 37.5 m, failure of the edge of the pillar does not occur (as evidenced by the absence of a stress relief zone); in other respects, the nature of the stress distribution is similar. An increase in the pillar width leads to a stress decrease.

In Figure 15, the dashed red line shows the compressive strength limit of coal at −13 MPa. The lines characterizing the stresses in the pillars with a width of 3.75 and 8.5 m are located below the compressive strength limit line. Therefore, these stresses exceed the strength limit of coal, which indicates a high risk of pillar failure. When the pillar width is 15 m or more, the stresses in the pillar do not reach the strength limit of the coal, which indicates the stability of the pillar. Thus, it can be concluded that with a pillar size of 15 m or more, the probability of its failure and the development of a pessimistic scenario of subsidence and overburden movement are extremely low. The authors understand that such an assessment of stability is simplified, since the pillar is located in a volumetric stress field and not in a uniaxial one. However, since the strength of coal under unconfined compression is higher than under uniaxial compression, as a first approximation, it can be assumed that the calculation was performed with a reasonable safety margin. More accurate assessments of the stability of the pillars require additional research.

The stability of the pillars between UCG reactors for thin coal seam conditions has not been studied previously, which highlights the novelty of this approach. However, the most closely related studies consider the following:

- Surface subsidence at a constant pillar width of 15 m with a seam thickness of 15 m, by Jiang et al. [31];
- Stability evaluation method of a gasification coal pillar at a constant pillar width of 16 m with a seam thickness of 5.0 m, by Tang et al. [64];
- The influence of wall curvature (different arch–depth ratios) on the reduction of the useful pillar's width, by Xu et al. [32] and Li et al. [33].

It is widely recognized that rock discontinuities (rock joints) play an important role in rock mass stability and affect the behavior of rock masses [65]. At the same time, understanding the characteristics of rock discontinuities plays a huge role in predicting stability [66]. However, the influence of rock joints was not considered in this study.

4.3. Simulation Discussion

Several conclusions can be drawn from the above analyses:

(1) The heat-affected zone of the UCG reactor is of insignificant size. In the study, the increase in temperature and, as a consequence, thermal stresses in the rocks near the cavity reactor were observed at a distance of up to 0.75 m into the roof and floor and up to 0.25 m into the coal seam. The gasification process has no direct impact on the stability of the surrounding rocks near previously extracted cavities.

(2) At the gasification stage, there is a high risk of failure of the coal seam near the UCG reactor. This can actually be interpreted as a reduction in the coal pillar width. In this study, the depth of coal failure in the wall side of the reactor cavity was 0.25 m, and the useful width of the pillar was reduced by 0.5 m. The analysis of pillar stability at the post-gasification stage should be carried out taking into account this reduction in the useful width of the pillar at the gasification stage.

(3) An increase in the pillar's width leads to a stress decrease in it. The optimization of pillar sizes consists of calculating its minimum width at which the stresses in the pillar do not exceed the strength of the coal. This will help to avoid the pessimistic scenario of surface subsidence and overburden movements with minimal coal losses in the pillar. For this study, the optimal pillar width was 15 m.

5. Conclusions

This study focused on the negative impact of coal gasification on overburden rock and the Earth's surface. Underground gasification of thin coal seams with the parallel CRIP method was studied. Multifield finite element analysis was conducted using ANSYS software to study the stress-strain state and temperature distribution in the surrounding rock. Based on the results of this investigation, the following conclusions can be drawn:

(1) Surface subsidence and rock movement above gasification cavities need to be within the pre-peak limits in the case of maintaining a safety pillar's bearing capacity. This ensures the low probability of a negative impact from the gasification process. For the conditions of this study, the gasification of a coal seam with a thickness of 1.05 m at a depth of 392–465 m, the surface subsidence did not exceed 46 mm with a pillar width of 3.75 m and 27 mm with a pillar width of 15.0 m. In this case, the height of the stress variation area above the gasification cavity does not exceed 70 m. The failure of the pillars between the reactor cavities leads to an increase in subsidence by 11.7 and 19.9 times for pillar widths of 3.75 m and 15.0 m, respectively. The overburden movement increases in a similar way. This puts aquifers and surface infrastructure at risk of destruction.

(2) The significant influence of the gasification process on the stability of the rock surrounding previously extracted cavities has not been established, since the size of the heat-affected zone of the UCG reactor is less than the thickness of the coal seam. At the gasification stage, there is a high risk of coal seam failure in the side walls of the UCG

reactor. This leads to a reduction in the useful width of the safety pillar. For the conditions of this study, the failure of coal at the gasification stage leads to a decrease in the useful pillar width by 0.5 m.

(3) To avoid the hazard of overburden rock and surface destruction caused by irreversible deformations with minimal coal losses, the width of the pillars should be optimized. The numerical experiment algorithm described in the paper can be used to optimize pillar width in any mining and geological conditions. For this study, the optimal pillar width was 15 m.

6. Limitations and Future Research

There are a number of limitations in this study. Firstly, unfortunately, this study does not contain the experimental validation of the results, since there is no possibility of such confirmation in the current circumstances. The article is aimed at increasing sustainability after achieving a just and sustainable peace in Ukraine. Secondly, this study does not experimentally confirm the insignificant size (as less than the coal seam thickness) of the heat-affected zone obtained using numerical simulation. The authors found confirmation in the studies of Otto and Kempka [54], Wang et al. [58], Xin et al. [59], and Sarhosis et al. [60]. In the future, the authors plan to conduct a sensitivity analysis of thermal extent for the rocks of the coal-bearing strata of the Ukrainian Donbass in laboratory conditions. Thirdly, the authors used the results of studies by Zhang et al. [55], Wu et al. [56], Sygała et al. [57], and Otto and Kempka [54] to determine the temperature-dependent properties of rock for the numerical model. Further research by the authors will be devoted to determining the influence of temperature on the mechanical properties of rocks of the coal-bearing strata of the Ukrainian Donbass.

Author Contributions: Conceptualization, I.S. and S.S.; methodology, I.S. and O.V.; software, I.S.; validation, I.S. and O.V.; formal analysis, S.S.; investigation, I.S.; resources, I.S.; writing—original draft preparation, I.S.; writing—review and editing, I.S. and S.S.; visualization, S.S.; supervision, I.S.; project administration, I.S. All authors have read and agreed to the published version of the manuscript.

Funding: This research received no external funding.

Institutional Review Board Statement: Not applicable.

Informed Consent Statement: Not applicable.

Data Availability Statement: The original contributions presented in the study are included in the article, further inquiries can be directed to the corresponding author.

Acknowledgments: The authors are grateful to the administration of Technical University "Metinvest Polytechnic" LLC. for supporting this research.

Conflicts of Interest: Authors were employed by the company Technical University "Metinvest Polytechnic" LLC. The authors declare that the research was conducted in the absence of any commercial or financial relationships that could be construed as a potential conflict of interest.

References

1. UNFCCC. Adoption of the Paris Agreement. Proposal by the President. United Nations Framework Convention on Climate Change. In Proceedings of the Conference of the Parties (COP21), Paris, France, 30 November–11 December 2015; pp. 1–31.
2. UNFCCC. Glasgow Climate Pact. In Proceedings of the Conference of the Parties Serving as the Meeting of the Parties to the Paris Agreement, Glasgow, UK, 31 October–13 November 2021; pp. 1–10. Available online: https://unfccc.int/sites/default/files/resource/cma2021_10_add1_adv.pdf (accessed on 1 July 2024).
3. Allam, Z.; Bibri, S.E.; Sharpe, S.A. The Rising Impacts of the COVID-19 Pandemic and the Russia–Ukraine War: Energy Transition, Climate Justice, Global Inequality, and Supply Chain Disruption. *Resources* **2022**, *11*, 99. [CrossRef]

4. BGR. Reserves, Resources and Availability of Energy Resources. Federal Institute for Geosciences and Natural Resources (BGR), Energy Study 2015. Available online: https://www.bgr.bund.de/EN/Themen/Energie/Downloads/energiestudie_2015_en.html (accessed on 10 December 2024).
5. Schiffer, H.-W.; Thielemann, T. Why there will be no peak coal in the foreseeable future. *Open J. Geol.* **2012**, *2*, 57–64. [CrossRef]
6. Tracking Coal-fired Electricity Generation. Available online: https://www.iea.org/energy-system/fossil-fuels/coal (accessed on 1 July 2024).
7. Bhutto, A.W.; Bazmi, A.A.; Zahedi, G. Underground coal gasification: From fundamentals to applications. *Prog. Energy Combust. Sci.* **2013**, *39*, 189–214. [CrossRef]
8. Burton, E.; Friedmann, J.; Upadhye, R. *Best Practices in Underground Coal Gasification*; Contract No. W-7405-Eng-48; Lawrence Livermore National Laboratory: Livermore, CA, USA, 2006.
9. Kempka, T.; Plötz, M.-L.; Schlüter, R.; Hamann, J.; Deowan, S.A.; Azzam, R. Carbon dioxide utilisation for carbamide production by application of the coupled UCG-urea process. *Energy Procedia* **2011**, *4*, 2200–2205. [CrossRef]
10. Nakaten, N.; Kötting, P.; Azzam, R.; Kempka, T. Underground Coal Gasification and CO_2 Storage Support Bulgaria's Low Carbon Energy Supply. *Energy Procedia* **2013**, *40*, 212–221. [CrossRef]
11. Lawrence Livermore National Laboratory (LLNL); Livermore, CA (United States). *Final Geometry and Dimensions of UCG Field Test Cavities*; Original Report Date: September 2012; Released as a Technical Report: 2017; USDOE National Nuclear Security Administration (NNSA): Kansas City, MI, USA, 2017.
12. Younger, P.L. Hydrogeological and Geomechanical Aspects of Underground Coal Gasification and its Direct Coupling to Carbon Capture and Storage. *Mine Water Environ.* **2011**, *30*, 127–140. [CrossRef]
13. Luo, Y.; Coertzen, M.; Dumble, S. Comparison of UCG Cavity Growth with CFD Model Predictions. In Proceedings of the Seventh International Conference on CFD in the Minerals and Process Industries CSIRO, Melbourne, Australia, 9–11 December 2009; pp. 1–5.
14. Elahi, S.M.; Chen, Z.; Nassir, M. Geomechanical Simulation of Underground Coal Gasification. In Proceedings of the 50th U.S. Rock Mechanics/Geomechanics Symposium, Houston, TX, USA, 26–29 June 2016; Volume 16, pp. 1–13.
15. Mostade, M. Underground Coal Gasification (UCG)—The Path to Commercialization. *CPSI J.* **2014**, *6*, 18–37.
16. Tian, H.; Kempka, T.; Xu, N.-X.; Ziegler, M. Physical Properties of Sandstones After High Temperature Treatment. *Rock Mech. Rock Eng.* **2012**, *45*, 1113–1117. [CrossRef]
17. Li, H.; Guo, G.; Zha, J.; Yuan, Y.; Zhao, B. Research on the surface movement rules and prediction method of underground coal gasification. *Bull. Eng. Geol. Environ.* **2016**, *75*, 1133–1142. [CrossRef]
18. Najafi, M.; Jalali, S.M.E.; KhaloKakaie, R. Thermal–mechanical–numerical analysis of stress distribution in the vicinity of underground coal gasification (UCG) panels. *Int. J. Coal Geol.* **2014**, *134–135*, 1–16. [CrossRef]
19. Li, H.; Guo, G.; Zheng, N. Influence of coal types on overlying strata movement and deformation in underground coal gasification without shaft and prediction method of surface subsidence. *Process. Saf. Environ. Prot.* **2018**, *120*, 302–312. [CrossRef]
20. Ranjith, P.G.; Viete, D.R.; Chen, B.J.; Samintha, M.; Perera, A. Transformation plasticity and the effect of temperature on the mechanical behaviour of Hawkesbury sandstone at atmospheric pressure. *Eng. Geol.* **2012**, *151*, 120–127. [CrossRef]
21. Zhang, W.; Sun, Q.; Hao, S.; Geng, J.; Lv, C. Experimental study on the variation of physicaland mechanical properties of rock after high temperature treatment. *Appl. Therm. Eng.* **2016**, *98*, 1297–1304. [CrossRef]
22. Wang, S.; Liao, H.; Chen, Y.; Fernández-Steeger, T.M.; Du, X.; Xiong, M.; Liao, S. Damage Evolution Constitutive Behavior of Rock in Thermo-Mechanical Coupling Processes. *Materials* **2021**, *14*, 7840. [CrossRef]
23. Ekneligoda, T.; Marshall, A. A coupled thermal-mechanical numerical model of underground coal gasification (UCG) including spontaneous coal combustion and its effects. *Int. J. Coal Geol.* **2018**, *199*, 31–38. [CrossRef]
24. Wang, X.; Zhang, Q.; Yuan, L. A coupled thermal-force-chemical-displacement multi-field model for underground coal gasification based on controlled retraction injection point technology and its thermal analysis. *Energy* **2024**, 130614. [CrossRef]
25. Yang, D.; Sarhosis, V.; Sheng, Y. Thermal–mechanical modelling around the cavities of underground coal gasification. *J. Energy Inst.* **2014**, *87*, 321–329. [CrossRef]
26. Zha, X.X.; Wang, H.Y.; Cheng, S.S. Finite element analysis of the subsidence of cap rocks during underground coal gasification process. *Adv. Mater. Res.* **2014**, *859*, 91–94. [CrossRef]
27. Lee, K.; Nam, J.; Park, J.; Hong, G. Numerical Analysis of Factors Influencing the Ground Surface Settlement Above a Cavity. *Materials* **2022**, *15*, 8301. [CrossRef]
28. Liu, X.; Xu, L.; Zhang, K. Strata movement characteristics in underground coal gasification (UCG) under thermal coupling and surface subsidence prediction methods. *Appl. Sci.* **2023**, *13*, 5192. [CrossRef]
29. Rezaei, M.; Rajabi, M. Vertical displacement estimation in roof and floor of an underground powerhouse cavern. *Eng. Fail. Anal.* **2018**, *90*, 290–309. [CrossRef]
30. Elahi, S.; Nassir, M.; Chen, Z. Effect of various coal constitutive models on coupled thermo-mechanical modeling of underground coal gasification. *J. Pet. Sci. Eng.* **2017**, *154*, 469–478. [CrossRef]

31. Jiang, Y.; Chen, B.; Teng, L.; Wang, Y.; Xiong, F. Surface Subsidence Modelling Induced by Formation of Cavities in Underground Coal Gasification. *Appl. Sci.* **2024**, *14*, 5733. [CrossRef]
32. Xu, Y.Y.; Li, H.Z.; Guo, G.L.; Liu, X.P. Stability analysis of hyperbolic coal pillars with peeling and high temperature effects. *Energy Explor. Exploit.* **2020**, *38*, 1574–1588. [CrossRef]
33. Li, H.; Guo, G.; Zha, J.; He, Y.; Wang, Z.; Qin, S. Stability evaluation method for hyperbolic coal pillars under the coupling effects of high temperature and ground stress. *Environ. Earth Sci.* **2017**, *76*, 704–714. [CrossRef]
34. Saik, P.; Dychkovskyi, R.; Lozynskyi, V.; Falshtynskyi, V.; Ovcharenko, A. Achieving climate neutrality in coal mining regions through the underground coal gasification. *E3S Web Conf.* **2024**, *526*, 01004. [CrossRef]
35. Saik, P.B.; Dychkovskyi, R.O.; Lozynskyi, V.H.; Malanchuk, Z.R.; Malanchuk, Y.Z. Revisiting the underground gasification of coal reserves from contiguous seams. *Nauk. Visn. NHU* **2016**, *6*, 60–66.
36. Seifi, M.; Chen, Z.; Abedi, J. Large scale simulation of UCG process applying porous medium approach. *Can. J. Chem. Eng.* **2015**, *93*, 1311–1325. [CrossRef]
37. Lozynskyi, V.; Falshtynskyi, V.; Kozhantov, A.; Kieush, L.; Saik, P. Increasing the underground coal gasification efficiency using preliminary electromagnetic coal mass heating. *IOP Conf. Ser. Earth Environ. Sci.* **2024**, *1348*, 012045. [CrossRef]
38. Sakhno, I.; Sakhno, S.; Petrenko, A.; Barkova, O.; Kobylianskyi, B. Numerical simulation of the surface subsidence evolution caused by the flooding of the longwall goaf during excavation of thin coal seams. *IOP Conf. Ser. Earth Environ. Sci.* **2023**, *1254*, 012057. [CrossRef]
39. Zhang, C.; Tu, S.; Zhao, Y. Compaction characteristics of the caving zone in a longwall goaf: A review. *Environ. Earth Sci.* **2019**, *78*, 27. [CrossRef]
40. Barla, G. Rock Anisotropy: Theory and Laboratory Testing (Chapter). In *Rock Mechanics*; Müller, L., Ed.; Springer: New York, NY, USA, 1972; pp. 131–169.
41. Cazacu, O.; Cristescu, N.D.; Shao, J.F.; Henry, J.P. A new anisotropicfailure criterion for transversely isotropic solids. *Mech. Cohesive-Frict. Mater.* **1998**, *3*, 89–103. [CrossRef]
42. Oka, F.; Kimoto, S.; Kobayashi, H.; Adachi, T. Anisotropic behaviorof soft sedimentary rock and a constitutive model. *Soils Found.* **2002**, *42*, 59–70. [CrossRef] [PubMed]
43. Khanlari, G.; Rafiei, B.; Abdilor, Y. Evaluation of strength anisotropy and failure modes of laminated sandstones. *Arab. J. Geosci.* **2015**, *8*, 3089–3102. [CrossRef]
44. Sakhno, I.G.; Molodetskyi, A.V.; Sakhno, S.V. Identification of material parameters for numerical simulation of the behavior ofrocks under true triaxial conditions. *Nauk. Visnyk NHU* **2018**, *5*, 48–53. [CrossRef]
45. Li, J.; Huang, Y.; Zhai, W.; Li, Y.; Ouyang, S.; Gao, H.; Li, W.; Ma, K.; Wu, L. Experimental study on acoustic emission of confined compression of crushed gangue under different loading rates: Disposal of gangue solid waste. *Sustainability* **2020**, *12*, 3911. [CrossRef]
46. Hoek, E.; Carranza-Torres, C.; Corkum, B. Hoek-Brown failure criterion—2002 edition. In Proceedings of the 5th North American Rock Mechanics Symposium and the 17th Tunnelling Association of Canada Conference, NARMS-TAC, Toronto, ON, Canada, 7–10 July 2002; pp. 267–271.
47. Hoek, E.; Diederichs, M. Empirical estimates of rock mass modulus. *Int. J. Rock Mech. Min. Sci.* **2006**, *43*, 203–215. [CrossRef]
48. Bieniawski, Z.T. *Engineering Rock Mass Classifications*; Wiley: New York, NY, USA, 1989.
49. Sakhno, I.; Sakhno, S.; Skrzypkowski, K.; Isaienkov, O.; Zagórski, K.; Zagórska, A. Floor Heave Control in Gob-Side Entry Retaining by Pillarless Coal Mining with Anti-Shear Pile Technology. *Appl. Sci.* **2024**, *14*, 4992. [CrossRef]
50. Tian, H.; Kempka, T.; Yu, S.; Ziegler, M. Mechanical Properties of Sandstones Exposed to High Temperature. *Rock Mech. Rock Eng.* **2015**, *49*, 321–327. [CrossRef]
51. Zheng, Y.; Zhang, L.; Wu, P.; Guo, X.; Li, M.; Zhu, F. Physical and Mechanical Properties and Damage Mechanism of Sandstone at High Temperatures. *Appl. Sci.* **2024**, *14*, 444. [CrossRef]
52. Xin, M.; Li, L.; Liu, C.; Xu, W.; Xie, M.; Han, J.; An, L. Change of sandstone microstructure and mineral transformation nearby UCG channel. *Fuel Process. Technol.* **2021**, *211*, 106575. [CrossRef]
53. Wang, G.; Yang, D.; Liu, S.; Fu, M.; Wang, L. Experimental Study on the Anisotropic Mechanical Properties of Oil Shales Under Real-Time High-Temperature Conditions. *Rock Mech. Rock Eng.* **2021**, *54*, 6565–6583. [CrossRef]
54. Otto, C.; Kempka, T. Thermo-Mechanical Simulations of Rock Behavior in Underground Coal Gasification Show Negligible Impact of Temperature-Dependent Parameters on Permeability Changes. *Energies* **2015**, *8*, 5800–5827. [CrossRef]
55. Zhang, L.; Mao, X.; Liu, R.; Guo, X.; Ma, D. The Mechanical Properties of Mudstone at High Temperatures: An Experimental Study. *Rock Mech. Rock Eng.* **2014**, *47*, 1479–1484. [CrossRef]
56. Wu, G.; Wang, Y.; Swift, G.; Chen, J. Laboratory Investigation of the Effects of Temperature on the Mechanical Properties of Sandstone. *Geotech. Geol. Eng.* **2013**, *31*, 809–816. [CrossRef]
57. Sygała, A.; Bukowska, M.; Janoszek, T. High temperature versus geomechanical parameters of selected rocks–the present state of research. *J. Sustain. Min.* **2013**, *12*, 45–51. [CrossRef]

58. Wang, P.; Deng, J.; Liu, W.; Xiao, Q.; Lv, Q.; Zhang, Y.; Hou, Y. Thermo-Mechanical Numerical Analysis of Stress and Damage Distribution within the Surrounding Rock of Underground Coal Gasification Panels. *Processes* **2023**, *11*, 2521. [CrossRef]
59. Xin, L.; Wang, B.; Li, J.; Niu, M.; Shang, Z.; Xu, W.; Wang, X.; Li, H. Modeling Test of Combustion Cavity Growth during Underground Coal Gasification in the Early Stage of Ignition. *ACS Omega* **2024**, *9*, 3691–3700. [CrossRef]
60. Sarhosis, V.; Yang, D.; Sheng, Y.; Kempka, T. Coupled hydro-thermal analysis of underground coal gasification reactor cool downfor subsequent CO_2 storage. *Energy Procedia* **2013**, *40*, 428–436. [CrossRef]
61. Yin, T.; Li, X.; Bin, W.; Yin, Z.; Jin, J. Mechanical properties of sandstones after high temperature under dynamic loading. *Chin. J. Geotech. Eng.* **2011**, *33*, 777–784.
62. Liu, S.; Bai, J.; Wang, X.; Wang, G.; Wu, B.; Li, Y.; Zhao, J. Study on the Stability of Coal Pillars Under the Disturbance of Repeated Mining in a Double-Roadway Layout System. *Front. Earth Sci.* **2021**, *9*, 754747. [CrossRef]
63. Jiang, L.; Zhang, P.; Chen, L.; Hao, Z.; Sainoki, A.; Mitri, H.S.; Wang, Q. Numerical Approach for Goaf-Side Entry Layout and Yield Pillar Design in Fractured Ground Conditions. *Rock Mech. Rock Eng.* **2017**, *50*, 3049–3071. [CrossRef]
64. Tang, C.; Li, H.; Guo, G.; Huang, W.; Chen, Y.; Huang, J.; Tang, L.; Yuan, Y.; Sun, J. Stability evaluation method of gasification coal pillar under thermal coupling condition for prevention of environment secondary pollution. *Sci. Total Environ.* **2024**, *954*, 176265. [CrossRef] [PubMed]
65. Krukovskyi, O.; Kurnosov, S.; Bulich, Y.; Yanzhula, O.; Demin, V. Substantiating the parameters for selecting a pillar width to protect permanent mine workings at great depths. Essays of Mining Science and Practice. *IOP Conf. Ser. Earth Environ. Sci.* **2022**, *970*, 012049. [CrossRef]
66. Chen, Q.; Ge, Y.; Tang, H. Rock Discontinuities Characterization from Large-Scale Point Clouds Using a Point-Based DeepLearning Method. *Eng. Geol.* **2024**, *337*, 107585. [CrossRef]